



# High-fidelity Metalens Imaging via Aberration Correcting Transformers

Byeonghyeon Lee<sup>1</sup>    Youbin Kim<sup>1</sup>    Yongjae Jo<sup>1</sup>    Hyunsu Kim<sup>1</sup>    Hyemi Park<sup>1</sup>  
 Yangkyu Kim<sup>1</sup>    Debabrata Mandal<sup>2</sup>    Praneeth Chakravarthula<sup>2†</sup>    Inki Kim<sup>1†</sup>  
 Eunbyung Park<sup>1†</sup>

<sup>1</sup> Sungkyunkwan University

<sup>2</sup> University of North Carolina at Chapel Hill

## Abstract

*Metalens is an emerging optical system with an irreplaceable merit in that it can be manufactured in ultra-thin and compact sizes, which shows great promise of various applications such as medical imaging and augmented/virtual reality (AR/VR). Despite its advantage in miniaturization, its practicality is constrained by severe aberrations and distortions, which significantly degrade the image quality. Several previous arts have attempted to address different types of aberrations, yet most of them are mainly designed for the traditional bulky lens and not convincing enough to remedy harsh aberrations of the metalens. While there have existed aberration correction methods specifically for metalens, they still fall short of restoration quality. In this work, we propose MetaFormer, an aberration correction framework for metalens-captured images, harnessing Vision Transformers (ViT) that has shown remarkable restoration performance in diverse image restoration tasks. Specifically, we devise a Multiple Adaptive Filters Guidance (MAFG), where multiple Wiener filters enrich the degraded input images with various noise-detail balances, enhancing output restoration quality. In addition, we introduce a Spatial and Transposed self-Attention Fusion (STAF) module, which aggregates features from spatial self-attention and transposed self-attention modules to further ameliorate aberration correction. We conduct extensive experiments, including correcting aberrated images and videos, and clean 3D reconstruction from the degraded images. The proposed method outperforms the previous arts by a significant margin. We further fabricate a metalens and verify the practicality of MetaFormer by restoring the images captured with the manufactured metalens in the wild. Code and pre-trained models are available at <https://benhenryl.github.io/MetaFormer>.*

<sup>†</sup>Corresponding authors.

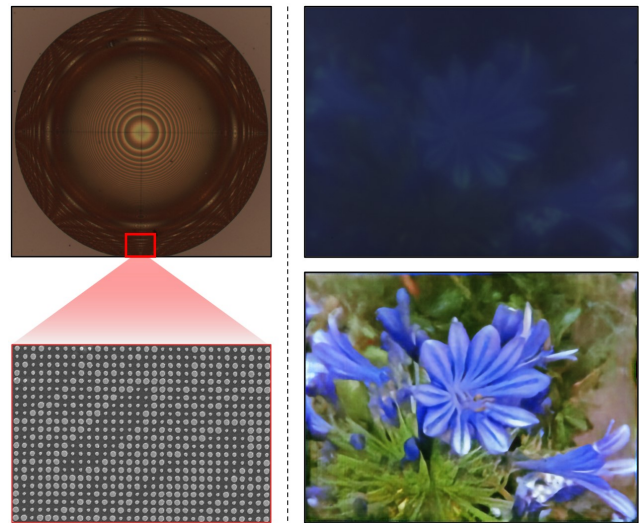


Figure 1. Left: The fabricated metalens. Right: An image captured with the manufactured metalens (top) and restored image with the proposed method (bottom).

## 1. Introduction

Metalens is an advanced optical device that leverages nanoscale engineering to manipulate light. Unlike traditional lenses relying on glass or plastic surfaces, the metalens harnesses a metasurface, a thin optical element consisting of nanostructures modulating optical properties such as phase, amplitude, and polarization. It can be fabricated in ultra-thin and compact sizes compared to the traditional bulky lens, making it an ideal option for various domains, including the medical industries, consumer electronics, and augmented/virtual reality (AR/VR) [31, 43, 52, 54, 67, 75, 87, 95]. Despite its great potential for miniaturization, existing metalenses have faced critical challenges, such as aberrations and distortions in the captured images, hampering their broad uses across diverse applications.

Aberrations in optical systems occur due to practical constraints and physical properties of lens materials. Dif-

ferent types of aberrations arise for different reasons, *e.g.* chromatic aberrations are produced when lights with different wavelengths refract at slightly different angles when they pass through a lens, resulting in being focused at different points. Another type of aberrations, spherical aberrations, occur when rays transmitting through the edges and center of the lens focus at different locations.

Several previous works [10, 23, 28] have attempted to correct these aberrations, primarily addressing them for general commercial cameras and not effective enough to mitigate intense aberrations of metalens. On the other hand, Tseng et al. [80] and Chakravarthula et al. [9] devised aberration correcting methods for the metalens. Tseng et al. [80] adopted convolutional neural networks (CNNs) and Chakravarthula et al. [9] employed a diffusion model [36, 74] for restoration. While promising, these methods have yet to reach the desired restoration quality.

Besides the aberration corrections, numerous studies have tackled other image degradations such as blur, noise, raindrops, haze, *etc.* A line of research introduced [39, 46, 47, 65] generative models [29, 36, 74] to produce clean images from degraded images, and other arts [32, 49, 60, 63, 91, 93] adopted CNNs. Another line of works [13, 16, 55, 81, 92] harnessed Vision Transformer (ViT) [22] for image restoration. Although they have shown prominent results, straightforwardly applying them to metalens-induced aberration correction is undesirable. This is because metalens can manipulate multiple optical properties, resulting in complex aberration patterns that vary in response to different wavelengths, which lead to severe chromatic aberrations. Moreover, aberrations in metalens images can amplify noise and distort intensity variations across channels. These aberrations are more complicated than the degradations encountered in conventional image restoration tasks, and those approaches devised for general image restoration lack in capacity to adapt to these distortions.

Among diverse frameworks, ViT-based approaches have proven effective for low-level computer vision tasks. ViT can effectively capture global context by leveraging a self-attention that allows each pixel in an image to communicate with all others, unlike CNNs, where pixels can interact only with neighboring pixels. This capability for modeling global relationships is especially crucial for image restoration, where understanding the overall structure plays a key role in removing noise or artifacts while preserving intricate details. Moreover, self-attention modules enable dynamic weighting of features, empowering the model to adaptively focus on the most relevant regions. While ViT has demonstrated its competence in various tasks, its potential for restoring metalens images remains largely unexplored.

It motivated us to propose MetaFormer, an aberration correction Transformer tailored for correcting the aberration of metalens-captured images. Particularly, we design a

Multiple Adaptive Filters Guidance (MAFG) that employs several Wiener filters [86], which have been widely used to reduce noise in signals. The advantages of MAFG are threefold: first, the representations deconvolved with different Wiener filters show diverse degrees of noise suppression and recovered fine details, allowing them to be processed complementarily in the restoration network. Secondly, MAFG provides a mechanism for handling unknown noise distributions. The Wiener filter penalizes noise based on the signal-to-noise ratio (SNR), which is usually obscure in real-world scenarios. By incorporating multiple Wiener filters with varied noise suppression parameters, MAFG can effectively address unknown noise distributions. Lastly, we adapt these parameters based on the image intensity, allowing for flexible handling across a broad range of images.

Furthermore, we extend Restormer [92] by incorporating both spatial and transposed self-attention and aggregating features from different attention modules, proposing a Spatial and Transposed self-Attention Fusion (STAF) module. Various previous arts [13, 16, 81] adopted encoder-decoder architecture with two types of attention mechanisms (spatial and transposed), but they apply them alternatively in both encoder and decoder, though they have different roles. The encoder focuses on capturing global structures, whereas the decoder emphasizes more on reconstructing fine details of images. Motivated by this, we implement spatial and transposed self-attention in parallel and fuse their features to guide the encoder in capturing global context and the decoder in enhancing fine reconstruction.

We conducted extensive experiments across various imaging scenarios to validate the effectiveness of the proposed MetaFormer. First, on synthetic aberrated images generated using point spread functions (PSF) from real metalenses, MetaFormer demonstrated notable performance improvements, outperforming the baseline model by 3.24 dB in PSNR and achieving state-of-the-art restoration quality across multiple evaluation metrics. Second, we extended and applied the proposed techniques to a video restoration model, where results further confirmed the proposed technique’s superiority in aberration correction in videos. Third, we tested MetaFormer on 3D reconstruction tasks using multi-view images (3D Gaussian Splatting [41]), demonstrating its capability to maintain both high-quality aberration correction and 3D consistency across views. Finally, we fabricated metalens using the open-source point spread function (PSF) of a metalens [80] and evaluated the proposed method on the images captured with the manufactured metalens. The corrected images demonstrated promising results, revealing new possibilities in metalens imaging.

To sum up, our contributions are as follows:

- We devise a Multiple Adaptive Filters Guidance (MAFG) that employs several Wiener filters operating adaptively to various images to enrich features of representations.

- We design a Spatial and Transposed self-Attention Fusion (STAF) module that applies spatial and transposed self-attention well aligned with encoder-decoder architecture.
- We fabricated a metalens with the open-source PSF and constructed a metalens-captured image dataset.
- We enhanced the baseline model by 3.24 dB in PSNR, accomplishing state-of-the-art restoration performance.

## 2. Related Works

### 2.1. Metalens

Recent advancements in nanofabrication have enabled the use of ultra-thin metasurfaces consisting of subwavelength scatterers that can independently adjust the amplitude, phase, and polarization of incident wavefronts, allowing for greater design flexibility [24, 27, 57, 62]. This flexibility has motivated research into applications such as flat meta-optics for imaging [2, 9, 12, 18, 27, 58, 80, 88], polarization control [4], and holography [97]. Notably, work by Tseng et al. [80] introduced a differentiable design for meta-optics achieving high image quality within a 0.5 mm aperture but with limitations in field performance beyond 40°. More recently, Chakravarthula et al. [9] introduced a metalens array design that enhances image quality across a full broadband spectrum over a 100° field of view (FoV) without increasing the back focal length, potentially allowing for one-step fabrication directly on the camera sensor coverglass. However, existing meta-optics still face challenges with chromatic and geometric aberrations, limiting broadband imaging capabilities [3, 57, 83, 88]. Although dispersion engineering methods have mitigated some chromatic aberrations [5, 42, 66, 73, 82], they remain restricted to very small apertures [68]. In this work, we introduce a framework to compensate for aberrations and overcome the challenges faced by such meta-optics imaging cameras.

### 2.2. Image Restoration models

Image restoration aims to recover high-quality images from degraded observations. Traditionally, Wiener deconvolution [86] recovered images by solving complex inverse problems. However, it often struggled with noise and complex degradations, limiting their real-world applications. Afterward, deep learning has revolutionized image restoration with data-driven methods. Vision Transformer, in particular, (ViT) [22] has achieved remarkable performances in image restoration tasks, including denoising [11, 26, 53, 81, 85, 92], deblurring [45, 59, 79, 85, 92], and super resolution [14–16, 55, 61, 77], by exploiting self-attention that can capture global interactions effectively.

Restormer [92] stood out with its superior performance, introducing transposed self-attention mechanisms that apply self-attention across the channel of an image, enabling efficient processing of high-resolution images. However,

it might limit the exploitation of spatial information. X-Restormer [13] further incorporated spatial self-attention mechanisms into Restormer to handle these shortcomings. This allowed the model to better capture spatial dependencies, still there is room for improvement in that it deployed attention blocks identically for encoder and decoder though they have different roles when learning the representation.

### 2.3. Aberration correction models

Optical aberration arises from imperfections in optical systems, with chromatic and spherical aberrations being frequently observed in the metalens imaging process. Chromatic aberration, where different wavelengths of light focus at different points, leads to color fringing, and spherical aberration occurs when the rays passing through the edges and center of the lens are focused at different points, resulting in blurriness. Extensive research has been conducted to correct these aberrations, and they can be broadly categorized into non-blind and blind aberration correction.

Non-blind approaches [17, 21, 33, 38, 40, 72, 96] require PSF calibration before training the models. Once the PSF is well calibrated, it can be consistently applied across various images, as optical aberrations are independent of the scene content in general [89, 90]. Especially, DWDN [21] leveraged Wiener deconvolution [86] in the feature space for multi-scale refinement and Li et al. [51] proposed a PSF-aware network using patch-wise deconvolution with deep priors to cope with spatially varying aberrations.

Blind aberration correction approaches [23, 28, 70, 71, 78, 90] correct aberrations through estimating aberration kernels and true images without any prior PSF information. Eboli et al. [23] adopted a small CNN for color correction, and Gong et al. [28] utilized the physical properties of lenses to improve image quality. These blind methods can be applied generally without demanding preprocess (*e.g.*, PSF calibration), but restoration quality may be unsatisfactory due to uncertainties when estimating PSF.

On the one hand, there have been aberration correction models designed for metalens imaging [9, 80]. Tseng et al. [80] employed CNNs and Wiener filters for restoration, but it struggled to restore the fine details of the image because of the limited receptive field of CNNs. Chakravarthula et al. [9] introduced diffusion models [36, 74] with Wiener filter to manage aberrations, yet it can introduce unrealistic details due to the stochasticity of the diffusion model.

Aberration correction poses unique challenges in the context of metalens imaging, but ViT has not been fully examined to address them. In this paper, we propose leveraging the ViT, adapting attention mechanisms to deal with complex aberration patterns in metalens imaging, to overcome the limitations faced by CNN and diffusion models.

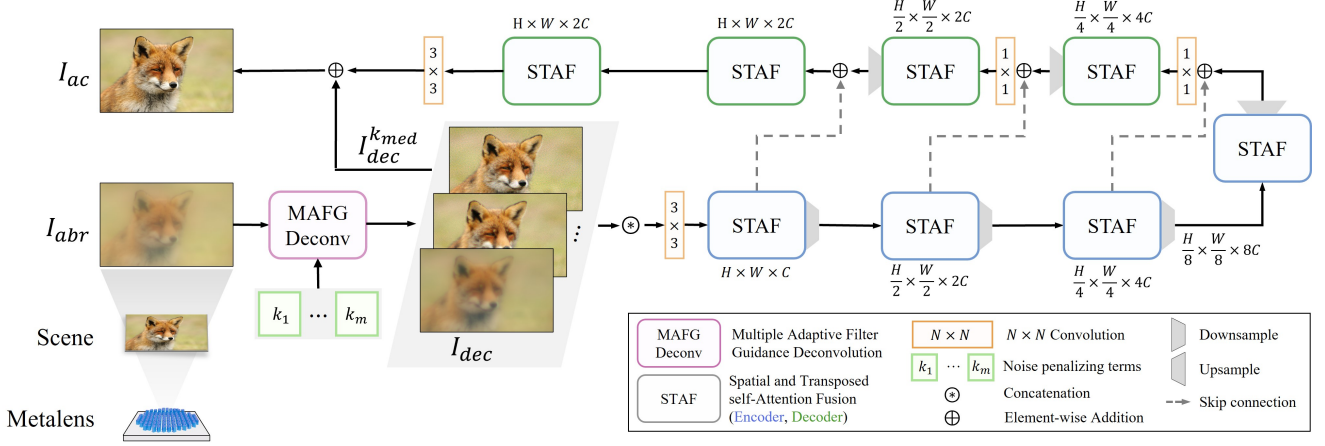


Figure 2. The overview of MetaFormer. It comprises Multiple Adaptive Filters Guidance (MAFG) which produces different representations with various noise-detail balances, and a Spatial and Transposed self-Attention Fusion (STAF) module that aggregates features differently in encoder and decoder.

### 3. Methods

Fig. 2 depicts the overall architecture of MetaFormer. It consists of Vision Transformer (ViT) as a backbone network for restoration (Sec. 3.2), Multiple Adaptive Filters Guidance (MAFG) (Sec. 3.3), and Spatial and Transposed self-Attention Fusion (STAF) blocks (Sec. 3.4). MetaFormer produces a residual image which is added to the input aberrated image to acquire the aberration-corrected image.

#### 3.1. Preliminary

**Metalens Imaging** An imaging formulation using a spatially invariant point spread function (PSF) can be written as follows<sup>1</sup>,

$$I_{abr} = I_c * PSF + n, \quad (1)$$

where  $*$  denotes the convolution operator, and  $I_{abr}$  is the observed image, which can be represented as the convolution of a clean image or an object  $I_c$  with a single PSF uniformly across the entire image. Then the noise  $n$ , such as shutter and natural noise, is added to generate the captured image  $I_{abr}$ . Convolution can be replaced with simple element-wise multiplication when  $I_c$  and  $PSF$  are in the frequency domains [8]. The PSF of metalens varies significantly with wavelength because different colors focus at different distances from the metalens. This produces color fringing and a low contrast in the captured image.

#### 3.2. Image Restoration using Vision Transformer

Chromatic aberrations of metalens differ across different wavelengths of light, implying that the aberrations affect each channel of the image distinctively. Vision Transformer (ViT) can model these channel-specific differences, leveraging their multi-head attention to process each channel

<sup>1</sup>While a more general approach involves a spatially varying PSF, this work focuses on restoring aberrated images using a spatially invariant PSF.

properly. Additionally, metalens-induced aberrations can degrade the images at various scales, affecting both high-frequency details (e.g., color fringes at sharp edges) and low-frequency components (e.g., gradual intensity shifts). ViT can represent multi-scale features, which can help in correcting different types of distortions.

As discussed, various ViT-based approaches [15, 16, 55, 59, 77, 81, 85, 92] have been developed for restoring images captured by traditional cameras. Among these, Restormer [92] has demonstrated remarkable restoration performance across multiple tasks, utilizing an encoder-decoder architecture with transposed self-attention (TA), a novel feed-forward network with gating mechanism [19], and depth-wise convolutions [37]. Nevertheless, applying Restormer directly to metalens image restoration does not yield satisfactory outcomes, as metalenses introduce more complex aberrations and distortions than conventional lenses, demanding a more sophisticated and tailored solution. Therefore, we employ Restormer as the backbone network and incorporate novel aberration-correcting modules to better align ViT with the specific challenges of metalens imaging. Additionally, we train ViT non-blindly, harnessing point spread function (PSF) for training, as the PSF for metalens can be easily obtained via calibration methods compared to the traditional cameras.

#### 3.3. Multiple Adaptive Filters Guidance

Before feeding the aberrated input images to the restoration network, we deconvolve the image first with multiple Wiener filters [86]. Wiener filter is a linear filter that has been used to reduce noise in signals, especially in the context of image processing and restoration [20, 21, 35, 69, 96, 98]. It minimizes the mean square error between the estimated and true signal, providing an optimal approach to reconstructing signals degraded by noise. It can also balance

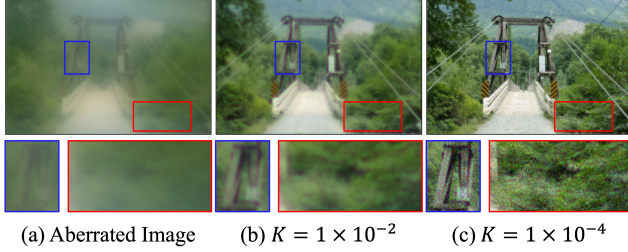


Figure 3. A comparison of the Wiener deconvolved images with different noise-penalization terms  $K$ . High  $K$  produces smooth representation (b), while smaller  $K$  results in a more textured but noisy representation (c).

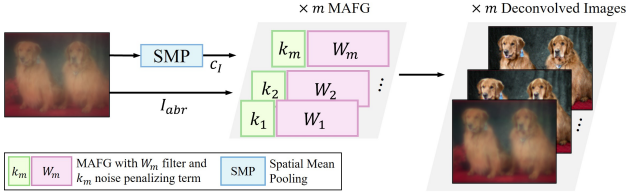


Figure 4. The process of Multiple Adaptive Filters Guidance (MAFG). It produces  $M$  different representations from the input images using  $M$  different Wiener filters.

noise suppression and detail preservation by exploiting the signal-to-noise ratio (SNR), which makes it particularly effective in image restoration tasks. Given a PSF, the Wiener filter in the frequency domain,  $W$ , is defined as follows,

$$W[u, v] = \frac{H^*[u, v]}{|H[u, v]|^2 + K}, \quad (2)$$

where  $[\cdot, \cdot]$  is an indexing operator, and  $u$  and  $v$  are horizontal and vertical spatial frequency respectively,  $H$  is a fourier transformed PSF,  $H^*$  is a complex conjugation of  $H$ , and  $K$  is an inverse of SNR. Note that each color channel has a different PSF, but we do not explicitly denote the channel for brevity, e.g.  $H_c$  or  $W_c$ .

As shown in Fig. 3,  $K$  plays a pivotal role in penalizing the noise; a greater  $K$  leads to a smoother representation, whereas a smaller  $K$  can preserve more high-frequency details, albeit with the increased noise. Inspired by this, we propose to use multiple Wiener filters to guide aberration correction with several distinct representations. It is not feasible to obtain an optimal Wiener filter with accurate SNR as noise distribution is unknown in the real world. Instead of estimating the noise distribution, we adopt multiple Wiener filters with different  $K$ . We use  $M$  Wiener filters and deconvolve the input image to yield  $M$  different representations—some focused on noise removal, others with fine information. Various representations are fed to the restoration model, and they can enrich the features complementarily, which in turn improves aberration correction.

Furthermore, we extend multiple Wiener filters to Multiple Adaptive Filters Guidance (MAFG), illustrated in Fig. 4,

which determines  $K$  adaptively considering the image intensity. Image with higher intensity tends to have better signal quality, so brighter channels often experience less noise and are less sensitive to noise [25]. Thus, we penalize noise less and capture more information for bright images by adjusting  $K$  with the image intensity. Also, we treat each channel differently to avoid suppressing high-SNR details unnecessarily. This is important when addressing metalens-captured images since metalens exhibit wavelength-dependent aberrations where each color channel suffers differently due to the different chromatic responses. Based on this observation, we slightly modify Eq. (2) for MAFG as follows:

$$W_m[u, v] = \frac{H^*[u, v]}{|H[u, v]|^2 + k_m \cdot (1 - c_I)}, \quad (3)$$

where  $m$  is the index of  $M$  different filters ( $1 \leq m \leq M$ ),  $c_I \in \mathbb{R}$  is the average intensity of each color channel, and  $k_m \in \mathbb{R}$  is a hyperparameter for scaling  $c_I$ . The proposed MAFG is adaptive to the input images, which allows flexible responses to the various images.

We obtain  $M$  different deconvolved images  $\{I_{dec}^m\}_{m=1}^M$  using MAFG with the following equation:

$$I_{dec}^m[x, y] = \text{ifft}(W_m \odot \text{fft}(I_{abr}))[x, y], \quad (4)$$

where  $\text{fft}$  and  $\text{ifft}$  are Fast Fourier Transform (FFT) and the inverse FFT [8], respectively. ‘ $\odot$ ’ is the Hadamard product,  $x$  and  $y$  are pixel coordinates.  $\{I_{dec}^m\}_{m=1}^M$  are concatenated along the channel dimension and fed to the restoration network. It is also worth mentioning that the MAFG can be applied to any other restoration model, including video restoration, with negligible computational costs.

### 3.4. Spatial and Transposed Self-Attention Fusion

As aforementioned, Restormer [92] relies solely on transposed self-attention to generate an attention map, often resulting in weak spatial context encoding. To improve context modeling, a variety of subsequent studies [13, 16, 81] leveraged both SA and TA, by alternatively applying them as depicted in Fig. 5 (a). In particular, X-Restormer [13] added spatial self-attention to Restormer and proved the enhanced spatial context encoding capability.

Nevertheless, there remains room for improvement, as existing methods apply SA and TA uniformly across both encoder and decoder stages despite their distinct objectives. The encoder primarily focuses on capturing a global context, emphasizing the overall structure and relationships within the images. This is critical in image restoration tasks since understanding the broader contexts helps identify patterns and features that may be corrupted in the degraded images. In contrast, the decoder mainly aims to recover local details and textures essential for high-fidelity restoration.

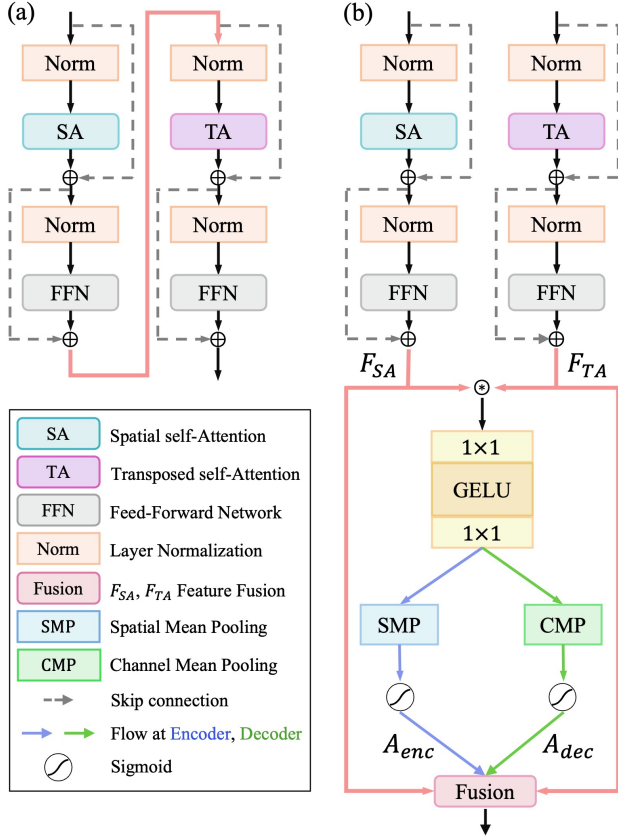


Figure 5. Comparison on applying SA and TA. (a). Previous works that apply SA and TA alternatively. (b). Proposed Spatial and Transposed self-Attention Fusion (STAF). It implements SA and TA in parallel and fuses features with different weights in the encoder and decoder.

Therefore, we propose a Spatial and Transposed self-Attention Fusion (STAF) module to further ameliorate image restoration. STAF implements SA and TA separately, not alternatively, and fuses SA and TA features with different weights in the encoder and decoder, as depicted in Fig. 5 (b). In detail, the outcome of SA and TA after feed-forward networks (denoted as  $F_{SA}, F_{TA} \in \mathbb{R}^{H \times W \times C}$ , respectively and  $H, W, C$  are height, width, and channel of the input feature) are concatenated along channel dimension to obtain concatenated feature  $F \in \mathbb{R}^{H \times W \times 2C}$ .  $F$  is then fed to a small CNN, consisting of two  $1 \times 1$  convolution layers with GELU activation [34], to mix features and halve channel dimension to  $C$ , and produce  $A \in \mathbb{R}^{H \times W \times C}$ , which is then treated differently in encoder and decoder. At the encoder side, we employ average pooling on spatial dimensions to efficiently reduce resolution while preserving crucial feature representations and apply the sigmoid function to  $A$  to obtain weight matrix  $A_{enc} \in \mathbb{R}^{1 \times 1 \times C}$ . On the other hand,  $W$  is averaged along the channel dimension to selectively emphasize the most relevant feature maps and apply the sigmoid function to produce weight matrix  $A_{dec} \in \mathbb{R}^{H \times W \times 1}$

for the decoder. This allows the decoder to prioritize different spatial areas, for instance, regions with more aberration can receive higher attention to be corrected. In a nutshell,  $A_{enc}$  and  $A_{dec}$  can be computed as follows:

$$\begin{aligned} F &= \text{Concat}(F_{SA}, F_{TA}), \\ A &= \text{Conv}(\text{GELU}(\text{Conv}(F))), \\ A_{enc} &= \sigma(\text{AVGPool}_{H,W}(A)), \\ A_{dec} &= \sigma(\text{AVGPool}_C(A)), \end{aligned} \quad (5)$$

where  $\sigma$  is the sigmoid activation, and  $\text{AVGPool}_{H,W}$  and  $\text{AVGPool}_C$  are average pooling along the height and width dimension and channel dimension, respectively.  $A_{enc}$  and  $A_{dec}$  are then used to compute the final feature of each block where  $F_{SA}$  and  $F_{TA}$  are mixed properly for the encoder and decoder with the equations:

$$\begin{aligned} F_{enc} &= F_{SA} \odot A_{enc} + F_{TA} \odot (1 - A_{enc}), \\ F_{dec} &= F_{SA} \odot A_{dec} + F_{TA} \odot (1 - A_{dec}), \end{aligned} \quad (6)$$

where  $\odot$  denotes the Hadamard product, and the index for each layer is omitted for brevity. The residual image obtained after passing through all STAF blocks is added to the  $I_{dec}^{k_{med}}$ , an image deconvolved with  $W_{k_{med}}$  where  $k_{med}$  is a median of  $k_m$ , to get the aberration-corrected image  $I_{ac}$ .

We adopted Overlapping Cross Attention (OCA), which partitions query matrix with non-overlapping windows and key and value matrices with overlapping windows, from HAT [15] for our SA module, following X-Restormer [13]. In addition, we employed the Gated-Deconv Feed-Forward network from Restormer [92] for our feed-forward network (FFN). However, any SA and FFN can be a valid option.

Fig. 6 shows the LAM [30] analysis which implies that STAF can restore the target region entailing more information, leading to better restoration quality. X-Restormer [13] also employs both SA and TA but aggregates the features in a simple manner, resulting in lacking information involvement and inferior aberration correction.

## 4. Experiments

### 4.1. Experimental Settings

We trained MetaFormer for 300K iterations with a batch size of 8 on 4 RTX A6000 GPUs. We set the number of filters  $M = 3$  and noise penalizing scalars  $k_1 = 1e - 2, k_2 = 1e - 3, k_3 = 3e - 4$ . We followed the overall experimental settings of Restormer [92] and X-Restormer [13]. Please refer to Restormer and X-Restormer for more details. We constructed synthetically aberrated datasets following Eq. (1) with metalens PSF from Tseng et al. [80], where  $n$  in Eq. (1) is a sum of two different per-pixel noises, Gaussian and Poisson noise.

We conducted experiments across various tasks: aberration correction on synthetic (Sec. 4.2) and real (Sec. 4.3) im-

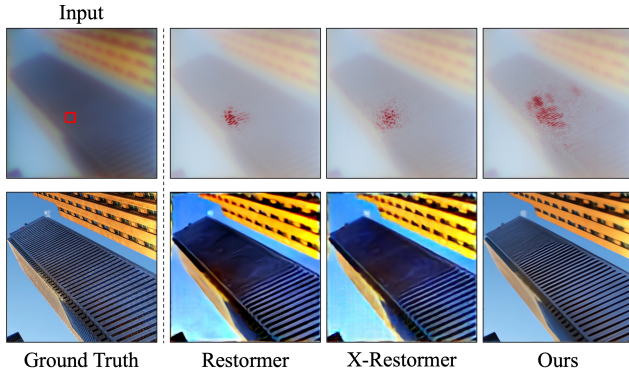


Figure 6. LAM [30] comparison over different models. Top: Input image and LAM analysis. Red marks in the images represent the pixels involved in restoring a target region, noted with a red box in the input image. Bottom: Restored results.

Method	PSNR $\uparrow$	SSIM $\uparrow$	LPIPS $\downarrow$
Wiener deconvolution [86]	25.08	0.6433	0.5164
Eboli et al. [23]	16.45	0.3602	0.8929
DWDN [21]	25.77	0.7320	0.3333
Tseng et al. [80]*	27.56	0.7612	0.3374
Restormer [92]	28.92	0.7719	0.3039
Ours	<b>32.16</b>	<b>0.8159</b>	<b>0.2810</b>

Table 1. Quantitative results on the aberrated Open Image V7 [7, 48] dataset. \* Its training dataset was not available, and the hyper-parameters for training were not clearly disclosed at the time of writing. Thus, we used the pre-trained weights for the evaluation.

ages, video aberration correction (Sec. 4.4), and 3D reconstruction with aberrated images (Sec. 4.4). Ablation studies are delivered in Sec. 4.6. Detailed experimental settings and more experimental results are described in the supplementary material.

## 4.2. Synthetic Image Aberration correction

We synthesized aberration on Open Image V7 [7, 48] dataset with PSF from Tseng et al. [80] and sampled 12K and 1K images for training and validation, respectively<sup>2</sup>. Tab. 1 and Fig. 7 describe the quantitative and qualitative results on the aberrated Open Image V7 dataset, respectively. Eboli et al. [23], a blind deconvolution approach, failed to compensate for the aberrations, and other baseline models, including Restormer [92], struggled with restoring fine details. Meanwhile, the proposed method could ameliorate Restormer with a noticeable margin and outperformed Tseng et al. [80] designed for metalens images.

## 4.3. Real Image Aberration Correction

We fabricated a metalens with the PSF from Tseng et al. [80] as shown in Fig. 1 (Left) and captured images to

<sup>2</sup>Training codes and pre-trained weights for Chakravarthula et al. [9] were not available, so we could only compare with Tseng et al. [80].

Method	PSNR $\uparrow$	SSIM $\uparrow$	LPIPS $\downarrow$
VRT [56]	16.38	0.4876	0.8058
VRT + MAFG	25.55	0.7795	<b>0.2347</b>
Restormer [92]	27.47	0.7463	0.2997
Ours	27.91	0.7798	0.2892
VRT w/ Ours	<b>28.00</b>	<b>0.8331</b>	0.2408

Table 2. Quantitative results on the aberrated DVD dataset [76].

Method	LLFF [64]			Tanks&Temples [44]		
	PSNR $\uparrow$	SSIM $\uparrow$	LPIPS $\downarrow$	PSNR $\uparrow$	SSIM $\uparrow$	LPIPS $\downarrow$
3D-GS [41]	15.34	0.3037	0.8706	14.85	0.2885	0.8641
3D-GS w/ Ours	24.07	0.6961	<b>0.2732</b>	22.25	0.6362	0.3259
3D-GS + Ours	<b>24.37</b>	<b>0.7009</b>	0.2867	<b>22.40</b>	<b>0.6427</b>	<b>0.3113</b>

Table 3. Quantitative results on the aberrated LLFF [64] and Tanks&Temples [44] dataset.

construct a real image dataset. It consists of 220 images, where 200 images are involved in fine-tuning the pre-trained MetaFormer, and 20 images are kept for validation. Fig. 1 (Right) shows the qualitative results on the metalens-captured images. Even though MetaFormer is trained only with the synthetic data, it can correct the aberration of the real image after fine-tuning with a small real dataset, which eases the cost of constructing a large-scale real image dataset. Please refer to the supplementary material for details about metalens fabrication, image capture setup, model fine-tuning, and more experimental results.

## 4.4. Video Aberration Correction

In this section, we assessed our method for the video aberration correction task. We employed VRT [56] as a baseline video restoration model and trained it with synthetically aberrated DVD [76] dataset. We incorporated the MAFG into VRT optimization (VRT + MAFG) and trained VRT with the output of pre-trained MetaFormer (VRT w/ Ours) from Sec. 4.2. Tab. 2 and Fig. 8 show that VRT struggled with correcting the aberration of the input video while simply applying the proposed MAFG to VRT (VRT + MAFG) could mitigate the severe aberration and restore the fine details. Furthermore, VRT trained with MetaFormer outputs (VRT w/ Ours) could enjoy both temporal consistency and clean representations, reaching the best restoration quality.

## 4.5. 3D Reconstruction with Aberrated Images

We further extended our method to clean 3D reconstruction, training 3D Gaussian Splatting (3D-GS) [41] with the sets of multi-view aberrated images. We embedded MetaFormer into 3D-GS training pipeline as delineated in Fig. 9. Specifically, we simulated aberration during 3D-GS training using Eq. (1) to constrain 3D-GS learning clean representations. The output ( $I_{ac}$ ) of the pre-trained MetaFormer, which is frozen during 3D-GS training, is in-

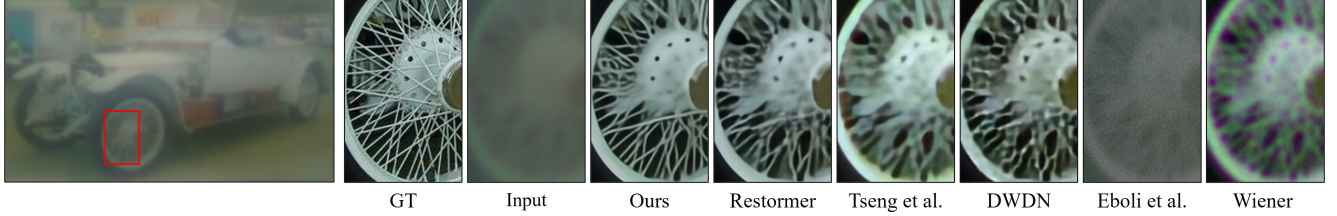


Figure 7. Qualitative results on the aberrated Open Image V7 [7, 48] dataset.



Figure 8. Qualitative results on the aberrated DVD [76] dataset.

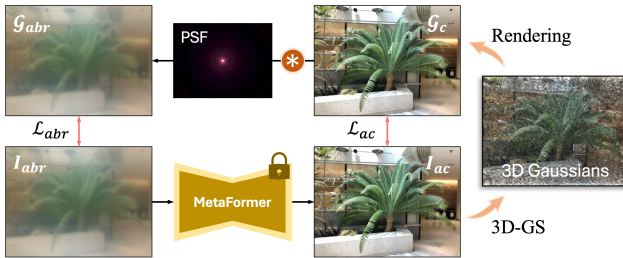


Figure 9. Training pipeline for MetaFormer embedded 3D-GS.

involved in supervising the rendered image ( $\mathcal{G}_c$ ) with a loss  $\mathcal{L}_{ac} = \mathcal{L}_{GS}(\mathcal{G}_c, I_{ac})$  where  $\mathcal{L}_{GS}$  is a reconstruction loss function defined in 3D-GS. The aberration-simulated image  $\mathcal{G}_{abr}$  is used to compute  $\mathcal{L}_{abr} = \mathcal{L}_{GS}(\mathcal{G}_{abr}, I_{abr})$ , with the training image  $I_{abr}$ . We use a sum of these losses to guide 3D-GS learning clean features from the aberrated images.

Tab. 3 and Fig. 10 provide the quantitative and qualitative results on the 3D reconstruction task, evaluated on LLFF [64] and Tanks&Temples [44] dataset, where we used *Truck* and *Train* data in Tanks&Temples dataset following 3D-GS. While 3D-GS fails to render clean images, the proposed pipeline that combines 3D-GS and MetaFormer (3D-GS + MetaFormer) shows sound reconstruction performance, even outperforming 3D-GS optimized with the restored output  $I_{ac}$  from MetaFormer (3D-GS w/ MetaFormer). This is because 3D-GS + MetaFormer can learn clean representation via  $\mathcal{L}_{ac}$  and meet the multi-view consistency with  $\mathcal{L}_{abr}$  simultaneously, resulting in better reconstruction quality.

#### 4.6. Ablation Studies

We conducted ablation studies of the proposed methods. Tab. 4 shows the comparison of MAFG and STAF module. Applying a single Wiener filter improved Restormer [92] by 1.80 dB in PSNR, but it elevated more when coupled with

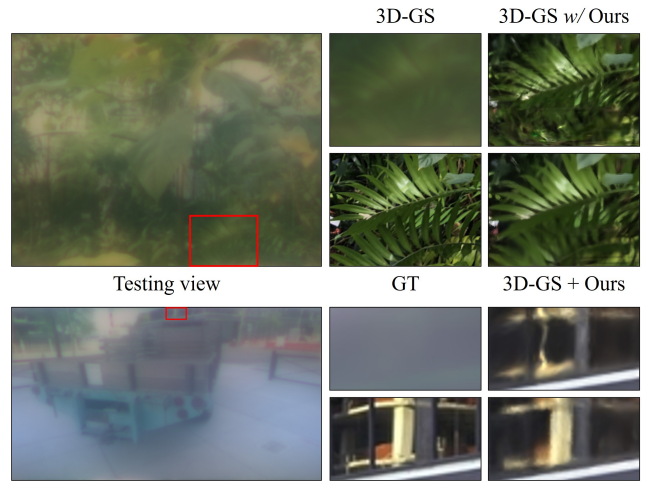


Figure 10. Qualitative results on the aberrated LLFF [64] (Top) and Tanks&Temples [44] (Bottom) dataset.

SWF	MAFG	STAF	PSNR $\uparrow$
			28.92
✓			30.72
	✓		32.00
	✓	✓	<b>32.16</b>

Table 4. Ablation study on the proposed methods. SWF stands for applying a single Wiener filter to Restormer [92].

MAFG and STAF. Other ablation studies are delivered in the supplementary material.

#### 5. Conclusion

We present MetaFormer, an aberration correcting transformer tailored for metalens imaging. We harness a Vision Transformer (ViT) that has not been fully explored in metalens imaging. We devise Multiple Adaptive Filters Guidance (MAFG) to enrich the feature of the aberration

correcting network. The proposed Spatial and Transposed self-Attention Fusion (STAF) module further boosts aberration correction by implementing SA and TA separately and fusing the outcomes differently in the encoder and decoder. The comprehensive experiments across diverse tasks covering correcting aberrated images, videos, and 3D reconstruction with aberrated images show the proposed method achieving state-of-the-art performance on various tasks. We also fabricate a metalens and restore the images captured in the wild, proving the practicality of MetaFormer.

## References

- [1] Eirikur Agustsson and Radu Timofte. Ntire 2017 challenge on single image super-resolution: Dataset and study. In *The IEEE Conference on Computer Vision and Pattern Recognition (CVPR) Workshops*, 2017. 15
- [2] Francesco Aieta, Patrice Genevet, Mikhail A. Kats, Nanfang Yu, Romain Blanchard, Zeno Gaburro, and Federico Capasso. Aberration-free ultrathin flat lenses and axicons at telecom wavelengths based on plasmonic metasurfaces. *Nano Letters*, 12(9):4932–4936, 2012. 3
- [3] Francesco Aieta, Mikhail A. Kats, Patrice Genevet, and Federico Capasso. Multiwavelength achromatic metasurfaces by dispersive phase compensation. *Science*, 347:1342–1345, 2015. 3
- [4] Amir Arbabi, Yu Horie, Mahmood Bagheri, and Andrei Faraon. Dielectric metasurfaces for complete control of phase and polarization with subwavelength spatial resolution and high transmission. *Nature Nanotechnology*, 10:937–943, 2015. 3
- [5] Ehsan Arbabi, Amir Arbabi, Seyede Mahsa Kamali, Yu Horie, and Andrei Faraon. Controlling the sign of chromatic dispersion in diffractive optics with dielectric metasurfaces. *Optica*, 4(6):625–632, 2017. 3
- [6] Jonathan T Barron, Ben Mildenhall, Dor Verbin, Pratul P Srinivasan, and Peter Hedman. Mip-nerf 360: Unbounded anti-aliased neural radiance fields. In *Proceedings of the IEEE/CVF conference on computer vision and pattern recognition*, pages 5470–5479, 2022. 14, 15, 19
- [7] Rodrigo Benenson and Vittorio Ferrari. From colouring-in to pointillism: revisiting semantic segmentation supervision. *arXiv preprint arXiv:2210.14142*, 2022. 7, 8, 14, 16, 17
- [8] EO Brigham. The fast fourier transform and its applications, 1988. 4, 5
- [9] Praneeth Chakravarthula, Jipeng Sun, Xiao Li, Chenyang Lei, Gene Chou, Mario Bijelic, Johannes Froesch, Arka Majumdar, and Felix Heide. Thin on-sensor nanophotonic array cameras. *ACM Transactions on Graphics (TOG)*, 42(6):1–18, 2023. 2, 3, 7
- [10] Joonyoung Chang, Hee Kang, and Moon Gi Kang. Correction of axial and lateral chromatic aberration with false color filtering. *IEEE Transactions on Image Processing*, 22(3): 1186–1198, 2012. 2
- [11] Hanting Chen, Yunhe Wang, Tianyu Guo, Chang Xu, Yiping Deng, Zhenhua Liu, Siwei Ma, Chunjing Xu, Chao Xu, and Wen Gao. Pre-trained image processing transformer. In *CVPR*, 2021. 3
- [12] Ji Chen, Xin Ye, Shenglun Gao, Yuxin Chen, Yunwei Zhao, Chunyu Huang, Kai Qiu, Shining Zhu, and Tao Li. Planar wide-angle-imaging camera enabled by metalens array. *Optica*, 9(4):431–437, 2022. 3
- [13] Xiangyu Chen, Zheyuan Li, Yuandong Pu, Yihao Liu, Jiantao Zhou, Yu Qiao, and Chao Dong. A comparative study of image restoration networks for general backbone network design. *arXiv preprint arXiv:2310.11881*, 2023. 2, 3, 5, 6
- [14] Xiangyu Chen, Xintao Wang, Jiantao Zhou, Yu Qiao, and Chao Dong. Activating more pixels in image super-resolution transformer. In *Proceedings of the IEEE/CVF Conference on Computer Vision and Pattern Recognition (CVPR)*, pages 22367–22377, 2023. 3
- [15] Xiangyu Chen, Xintao Wang, Jiantao Zhou, Yu Qiao, and Chao Dong. Activating more pixels in image super-resolution transformer. In *Proceedings of the IEEE/CVF conference on computer vision and pattern recognition*, pages 22367–22377, 2023. 4, 6
- [16] Zheng Chen, Yulun Zhang, Jinjin Gu, Linghe Kong, Xiaokang Yang, and Fisher Yu. Dual aggregation transformer for image super-resolution. In *Proceedings of the IEEE/CVF international conference on computer vision*, pages 12312–12321, 2023. 2, 3, 4, 5
- [17] Sunghyun Cho, Jue Wang, and Seungyong Lee. Handling outliers in non-blind image deconvolution. In *2011 International Conference on Computer Vision*, pages 495–502. IEEE, 2011. 3
- [18] Shane Colburn, Alan Zhan, and Arka Majumdar. Metasurface optics for full-color computational imaging. *Science Advances*, 4:eaar2114, 2018. 3
- [19] Yann N Dauphin, Angela Fan, Michael Auli, and David Grangier. Language modeling with gated convolutional networks. In *International conference on machine learning*, pages 933–941. PMLR, 2017. 4
- [20] Jiangxin Dong, Stefan Roth, and Bernt Schiele. Deep wiener deconvolution: Wiener meets deep learning for image deblurring. *Advances in Neural Information Processing Systems*, 33:1048–1059, 2020. 4
- [21] Jiangxin Dong, Stefan Roth, and Bernt Schiele. Dwdn: Deep wiener deconvolution network for non-blind image deblurring. *IEEE Transactions on Pattern Analysis and Machine Intelligence*, 44(12):9960–9976, 2021. 3, 4, 7
- [22] Alexey Dosovitskiy. An image is worth 16x16 words: Transformers for image recognition at scale. *arXiv preprint arXiv:2010.11929*, 2020. 2, 3
- [23] Thomas Eboli, Jean-Michel Morel, and Gabriele Facciolo. Fast two-step blind optical aberration correction. In *European Conference on Computer Vision*, pages 693–708. Springer, 2022. 2, 3, 7
- [24] Jacob Engelberg and Uriel Levy. The advantages of metalenses over diffractive lenses. *Nature Communications*, 11: 1991, 2020. 3
- [25] Baris I Erkmen and Jeffrey H Shapiro. Signal-to-noise ratio of gaussian-state ghost imaging. *Physical Review A—Atomic, Molecular, and Optical Physics*, 79(2):023833, 2009. 5

- [26] Chi-Mao Fan, Tsung-Jung Liu, and Kuan-Hsien Liu. Sunet: swin transformer unet for image denoising. In *2022 IEEE International Symposium on Circuits and Systems (ISCAS)*, pages 2333–2337. IEEE, 2022. 3
- [27] Johannes E Fröch, Praneeth K Chakravarthula, Jipeng Sun, Ethan Tseng, Shane Colburn, Alan Zhan, Forrest Miller, Anna Wirth-Singh, Quentin AA Tanguy, Zheyi Han, et al. Beating bandwidth limits for large aperture broadband nano-optics. *arXiv preprint arXiv:2402.06824*, 2024. 3
- [28] Jin Gong, Runzhao Yang, Weihang Zhang, Jinli Suo, and Qionghai Dai. A physics-informed low-rank deep neural network for blind and universal lens aberration correction. In *Proceedings of the IEEE/CVF Conference on Computer Vision and Pattern Recognition*, pages 24861–24870, 2024. 2, 3
- [29] Ian Goodfellow, Jean Pouget-Abadie, Mehdi Mirza, Bing Xu, David Warde-Farley, Sherjil Ozair, Aaron Courville, and Yoshua Bengio. Generative adversarial networks. *Communications of the ACM*, 63(11):139–144, 2020. 2
- [30] Jinjin Gu and Chao Dong. Interpreting super-resolution networks with local attribution maps. In *Proceedings of the IEEE/CVF Conference on Computer Vision and Pattern Recognition*, pages 9199–9208, 2021. 6, 7
- [31] Tian Gu, Hyun Jung Kim, Clara Rivero-Baleine, and Juejun Hu. Reconfigurable metasurfaces towards commercial success. *Nature Photonics*, 17(1):48–58, 2023. 1
- [32] Jingwen He, Chao Dong, and Yu Qiao. Modulating image restoration with continual levels via adaptive feature modification layers. In *The IEEE Conference on Computer Vision and Pattern Recognition (CVPR)*, 2019. 2
- [33] Felix Heide, Mushfiqur Rouf, Matthias B Hullin, Bjorn Labitzke, Wolfgang Heidrich, and Andreas Kolb. High-quality computational imaging through simple lenses. *ACM Transactions on Graphics (ToG)*, 32(5):1–14, 2013. 3
- [34] Dan Hendrycks and Kevin Gimpel. Gaussian error linear units (gelus). *arXiv preprint arXiv:1606.08415*, 2016. 6
- [35] AD Hiller and Roland T Chin. Iterative wiener filters for image restoration. In *International Conference on Acoustics, Speech, and Signal Processing*, pages 1901–1904. IEEE, 1990. 4
- [36] Jonathan Ho, Ajay Jain, and Pieter Abbeel. Denoising diffusion probabilistic models. *Advances in neural information processing systems*, 33:6840–6851, 2020. 2, 3
- [37] Andrew G Howard. Mobilenets: Efficient convolutional neural networks for mobile vision applications. *arXiv preprint arXiv:1704.04861*, 2017. 4
- [38] Neel Joshi, Richard Szeliski, and David J Kriegman. Psf estimation using sharp edge prediction. In *2008 IEEE Conference on Computer Vision and Pattern Recognition*, pages 1–8. IEEE, 2008. 3
- [39] Bahjat Kawar, Michael Elad, Stefano Ermon, and Jiaming Song. Denoising diffusion restoration models. *Advances in Neural Information Processing Systems*, 35:23593–23606, 2022. 2
- [40] Eric Kee, Sylvain Paris, Simon Chen, and Jue Wang. Modeling and removing spatially-varying optical blur. In *2011 IEEE international conference on computational photography (ICCP)*, pages 1–8. IEEE, 2011. 3
- [41] Bernhard Kerbl, Georgios Kopanas, Thomas Leimkühler, and George Drettakis. 3d gaussian splatting for real-time radiance field rendering. *ACM Trans. Graph.*, 42(4):139–1, 2023. 2, 7, 14, 15
- [42] Mohammadreza Khorasaninejad, Zhujun Shi, Alexander Y Zhu, Wei-Ting Chen, Vyshakh Sanjeev, Aun Zaidi, and Federico Capasso. Achromatic metalens over 60 nm bandwidth in the visible and metalens with reverse chromatic dispersion. *Nano Letters*, 17(3):1819–1824, 2017. 3
- [43] Sun-Je Kim, Changhyun Kim, Youngjin Kim, Jinsoo Jeong, Seokho Choi, Woojun Han, Jaisoon Kim, and Byoungsoo Lee. Dielectric metalens: properties and three-dimensional imaging applications. *Sensors*, 21(13):4584, 2021. 1
- [44] Arno Knapitsch, Jaesik Park, Qian-Yi Zhou, and Vladlen Koltun. Tanks and temples: Benchmarking large-scale scene reconstruction. *ACM Transactions on Graphics (ToG)*, 36(4):1–13, 2017. 7, 8, 14
- [45] Lingshun Kong, Jiangxin Dong, Mingqiang Li, Jianjun Ge, and Jinshan Pan. Efficient frequency domain-based transformers for high-quality image deblurring, 2022. 3
- [46] Orest Kupyn, Volodymyr Budzan, Mykola Mykhailych, Dmytro Mishkin, and Jiří Matas. Deblurgan: Blind motion deblurring using conditional adversarial networks. In *Proceedings of the IEEE conference on computer vision and pattern recognition*, pages 8183–8192, 2018. 2
- [47] Orest Kupyn, Tetiana Martyniuk, Junru Wu, and Zhangyang Wang. Deblurgan-v2: Deblurring (orders-of-magnitude) faster and better. In *Proceedings of the IEEE/CVF international conference on computer vision*, pages 8878–8887, 2019. 2
- [48] Alina Kuznetsova, Hassan Rom, Neil Alldrin, Jasper Uijlings, Ivan Krasin, Jordi Pont-Tuset, Shahab Kamali, Stefan Popov, Matteo Mallocci, Alexander Kolesnikov, et al. The open images dataset v4: Unified image classification, object detection, and visual relationship detection at scale. *International journal of computer vision*, 128(7):1956–1981, 2020. 7, 8, 14, 16, 17
- [49] Bruno Lecouat, Jean Ponce, and Julien Mairal. Fully trainable and interpretable non-local sparse models for image restoration. *Proc. European Conference on Computer Vision (ECCV)*, 2020. 2
- [50] Byeonghyeon Lee, Howoong Lee, Xiangyu Sun, Usman Ali, and Eunbyung Park. Deblurring 3d gaussian splatting. *arXiv preprint arXiv:2401.00834*, 2024. 14
- [51] Xiu Li, Jinli Suo, Weihang Zhang, Xin Yuan, and Qionghai Dai. Universal and flexible optical aberration correction using deep-prior based deconvolution. In *Proceedings of the IEEE/CVF International Conference on Computer Vision*, pages 2613–2621, 2021. 3
- [52] Yan Li, Shuyi Chen, Haowen Liang, Xiuying Ren, Lingcong Luo, Yuye Ling, Shuxin Liu, Yikai Su, and Shin-Tson Wu. Ultracompact multifunctional metalens visor for augmented reality displays. *PhotonIX*, 3(1):29, 2022. 1
- [53] Yawei Li, Yuchen Fan, Xiaoyu Xiang, Denis Demandolx, Rakesh Ranjan, Radu Timofte, and Luc Van Gool. Efficient and explicit modelling of image hierarchies for image restoration. In *Proceedings of the IEEE/CVF Conference*

- on *Computer Vision and Pattern Recognition*, pages 18278–18289, 2023. 3
- [54] Zhaoyi Li, Peng Lin, Yao-Wei Huang, Joon-Suh Park, Wei Ting Chen, Zhujun Shi, Cheng-Wei Qiu, Ji-Xin Cheng, and Federico Capasso. Meta-optics achieves rgb-achromatic focusing for virtual reality. *Science Advances*, 7(5): eabe4458, 2021. 1
- [55] Jingyun Liang, Jiezhong Cao, Guolei Sun, Kai Zhang, Luc Van Gool, and Radu Timofte. Swinir: Image restoration using swin transformer. In *Proceedings of the IEEE/CVF international conference on computer vision*, pages 1833–1844, 2021. 2, 3, 4
- [56] Jingyun Liang, Jiezhong Cao, Yuchen Fan, Kai Zhang, Rakesh Ranjan, Yawei Li, Radu Timofte, and Luc Van Gool. Vrt: A video restoration transformer. *IEEE Transactions on Image Processing*, 2024. 7
- [57] Dianmin Lin, Pengyu Fan, Erez Hasman, and Mark L. Brongersma. Dielectric gradient metasurface optical elements. *Science*, 345(6194):298–302, 2014. 3
- [58] Zin Lin, Charles Roques-Carmes, Raphaël Pestourie, Marin Soljačić, Arka Majumdar, and Steven G. Johnson. End-to-end nanophotonic inverse design for imaging and polarimetry. *Nanophotonics*, 10(3):1177–1187, 2021. 3
- [59] Hanzhou Liu, Binghan Li, Chengkai Liu, and Mi Lu. De-blurinat: A lightweight and effective transformer for image deblurring, 2024. 3, 4
- [60] Pengju Liu, Hongzhi Zhang, Lian Wei, and Wangmeng Zuo. Multi-level wavelet convolutional neural networks. *IEEE Access*, 7:74973–74985, 2019. 2
- [61] Zhisheng Lu, Juncheng Li, Hong Liu, Chaoyan Huang, Linlin Zhang, and Tiejong Zeng. Transformer for single image super-resolution, 2022. 3
- [62] Joseph N. Mait, Ravindra A. Athale, Joseph van der Gracht, and Gary W. Euliss. Potential applications of metamaterials to computational imaging. In *Proc. Frontiers in Optics / Laser Science*, page FTu8B.1, 2020. 3
- [63] Xiao-Jiao Mao, Chunhua Shen, and Yubin Yang. Image restoration using very deep convolutional encoder-decoder networks with symmetric skip connections. In *Neural Information Processing Systems*, 2016. 2
- [64] Ben Mildenhall, Pratul P. Srinivasan, Rodrigo Ortiz-Cayon, Nima Khademi Kalantari, Ravi Ramamoorthi, Ren Ng, and Abhishek Kar. Local light field fusion: Practical view synthesis with prescriptive sampling guidelines. *ACM Transactions on Graphics (TOG)*, 2019. 7, 8, 14
- [65] Naoki Murata, Koichi Saito, Chieh-Hsin Lai, Yuhta Takida, Toshimitsu Uesaka, Yuki Mitsufuji, and Stefano Ermon. Gibbsddrm: A partially collapsed gibbs sampler for solving blind inverse problems with denoising diffusion restoration. In *International conference on machine learning*, pages 25501–25522. PMLR, 2023. 2
- [66] A. Ndao, Li-Yi Hsu, Jeongho Ha, Junhee Park, C. Chang-Hasnain, and B. Kanté. Octave bandwidth photonic fishnet-achromatic-metalens. *Nature Communications*, 11:3205, 2020. 3
- [67] Joon-Suh Park, Shuyan Zhang, Alan She, Wei Ting Chen, Peng Lin, Kerolos MA Yousef, Ji-Xin Cheng, and Federico Capasso. All-glass, large metalens at visible wavelength using deep-ultraviolet projection lithography. *Nano letters*, 19(12):8673–8682, 2019. 1
- [68] Federico Presutti and Francesco Monticone. Focusing on bandwidth: achromatic metalens limits. *Optica*, 7(6):624–631, 2020. 3
- [69] Valeriya Pronina, Filippos Kokkinos, Dmitry V Dylov, and Stamatios Lefkimmiatis. Microscopy image restoration with deep wiener-kolmogorov filters. In *Computer Vision—ECCV 2020: 16th European Conference, Glasgow, UK, August 23–28, 2020, Proceedings, Part XX 16*, pages 185–201. Springer, 2020. 4
- [70] Kambiz Rahbar and Karim Faez. Blind correction of lens aberration using zernike moments. In *2011 18th IEEE International Conference on Image Processing*, pages 861–864. IEEE, 2011. 3
- [71] Christian J Schuler, Michael Hirsch, Stefan Harmeling, and Bernhard Schölkopf. Blind correction of optical aberrations. In *Computer Vision—ECCV 2012: 12th European Conference on Computer Vision, Florence, Italy, October 7–13, 2012, Proceedings, Part III 12*, pages 187–200. Springer, 2012. 3
- [72] Yichang Shih, Brian Guenter, and Neel Joshi. Image enhancement using calibrated lens simulations. In *Computer Vision—ECCV 2012: 12th European Conference on Computer Vision, Florence, Italy, October 7–13, 2012, Proceedings, Part IV 12*, pages 42–56. Springer, 2012. 3
- [73] Sajan Shrestha, Adam C. Overvig, Ming Ying Lu, Aaron Stein, and Nanfang Yu. Broadband achromatic dielectric metalenses. *Light: Science & Applications*, 7:85, 2018. 3
- [74] Jiaming Song, Chenlin Meng, and Stefano Ermon. Denoising diffusion implicit models. *arXiv preprint arXiv:2010.02502*, 2020. 2, 3
- [75] Endri Stoja, Simon Konstandin, Dennis Philipp, Robin N Wilke, Diego Betancourt, Thomas Bertuch, Jürgen Jenne, Reiner Umathum, and Matthias Günther. Improving magnetic resonance imaging with smart and thin metasurfaces. *Scientific reports*, 11(1):16179, 2021. 1
- [76] Shuo Chen Su, Mauricio Delbracio, Jue Wang, Guillermo Sapiro, Wolfgang Heidrich, and Oliver Wang. Deep video deblurring for hand-held cameras. In *Proceedings of the IEEE conference on computer vision and pattern recognition*, pages 1279–1288, 2017. 7, 8, 14, 19
- [77] Long Sun, Jiangxin Dong, Jinhui Tang, and Jinshan Pan. Spatially-adaptive feature modulation for efficient image super-resolution. In *ICCV*, 2023. 3, 4
- [78] Huixuan Tang and Kiriakos N Kutulakos. What does an aberrated photo tell us about the lens and the scene? In *IEEE International Conference on Computational Photography (ICCP)*, pages 1–10. IEEE, 2013. 3
- [79] Fu-Jen Tsai, Yan-Tsung Peng, Yen-Yu Lin, Chung-Chi Tsai, and Chia-Wen Lin. Stripformer: Strip transformer for fast image deblurring. In *ECCV*, 2022. 3
- [80] Ethan Tseng, Shane Colburn, James Whitehead, Luocheng Huang, Seung-Hwan Baek, Arka Majumdar, and Felix Heide. Neural nano-optics for high-quality thin lens imaging. *Nature communications*, 12(1):6493, 2021. 2, 3, 6, 7, 13

- [81] Zhijun Tu, Kunpeng Du, Hanting Chen, Hailing Wang, Wei Li, Jie Hu, and Yunhe Wang. Ipt-v2: Efficient image processing transformer using hierarchical attentions. *arXiv preprint arXiv:2404.00633*, 2024. 2, 3, 4, 5
- [82] Shuming Wang, Pin Chieh Wu, Vin-Cent Su, Yi-Chieh Lai, Cheng Hung Chu, Jia-Wern Chen, Shen-Hung Lu, Ji Chen, Beibei Xu, Chieh-Hsiung Kuan, et al. Broadband achromatic optical metasurface devices. *Nature Communications*, 8(1): 187, 2017. 3
- [83] Shuming Wang, Pin Chieh Wu, Vin-Cent Su, Yi-Chieh Lai, Mu-Ku Chen, Hsin Yu Kuo, Bo Han Chen, Yu Han Chen, Tzu-Ting Huang, Jung-Hsi Wang, Ray-Ming Lin, Chieh-Hsiung Kuan, Tao Li, Zhen lin Wang, Shining Zhu, and Din Ping Tsai. A broadband achromatic metalens in the visible. *Nature Nanotechnology*, 13:227–232, 2018. 3
- [84] Zhou Wang, Alan C Bovik, Hamid R Sheikh, and Eero P Simoncelli. Image quality assessment: from error visibility to structural similarity. *IEEE transactions on image processing*, 13(4):600–612, 2004. 13
- [85] Zhendong Wang, Xiaodong Cun, Jianmin Bao, Wengang Zhou, Jianzhuang Liu, and Houqiang Li. Uformer: A general u-shaped transformer for image restoration. In *Proceedings of the IEEE/CVF Conference on Computer Vision and Pattern Recognition (CVPR)*, pages 17683–17693, 2022. 3, 4
- [86] Norbert Wiener. *Extrapolation, interpolation, and smoothing of stationary time series: with engineering applications*. The MIT press, 1949. 2, 3, 4, 7
- [87] Gwanho Yoon, Kwan Kim, Se-Um Kim, Seunghoon Han, Heon Lee, and Junsuk Rho. Printable nanocomposite metalens for high-contrast near-infrared imaging. *ACS nano*, 15(1):698–706, 2021. 1
- [88] Nanfang Yu and Federico Capasso. Flat optics with designer metasurfaces. *Nature Materials*, 13:139–150, 2014. 3
- [89] Tao Yue, Jinli Suo, Yudong Xiao, Lei Zhang, and Qionghai Dai. Image quality enhancement using original lens via optical computing. *Optics express*, 22(24):29515–29530, 2014. 3
- [90] Tao Yue, Jinli Suo, Jue Wang, Xun Cao, and Qionghai Dai. Blind optical aberration correction by exploring geometric and visual priors. In *Proceedings of the IEEE Conference on Computer Vision and Pattern Recognition*, pages 1684–1692, 2015. 3
- [91] Syed Waqas Zamir, Aditya Arora, Salman Khan, Munawar Hayat, Fahad Shahbaz Khan, Ming-Hsuan Yang, and Ling Shao. Multi-stage progressive image restoration. In *CVPR*, 2021. 2
- [92] Syed Waqas Zamir, Aditya Arora, Salman Khan, Munawar Hayat, Fahad Shahbaz Khan, and Ming-Hsuan Yang. Restormer: Efficient transformer for high-resolution image restoration. In *Proceedings of the IEEE/CVF conference on computer vision and pattern recognition*, pages 5728–5739, 2022. 2, 3, 4, 5, 6, 7, 8, 14, 15
- [93] Kai Zhang, Wangmeng Zuo, Shuhang Gu, and Lei Zhang. Learning deep cnn denoiser prior for image restoration. In *IEEE Conference on Computer Vision and Pattern Recognition*, pages 3929–3938, 2017. 2
- [94] Richard Zhang, Phillip Isola, Alexei A Efros, Eli Shechtman, and Oliver Wang. The unreasonable effectiveness of deep features as a perceptual metric. In *Proceedings of the IEEE conference on computer vision and pattern recognition*, pages 586–595, 2018. 14
- [95] Shuyan Zhang, Chi Lok Wong, Shuwen Zeng, Renzhe Bi, Kolvyn Tai, Kishan Dholakia, and Malini Olivo. Metasurfaces for biomedical applications: imaging and sensing from a nanophotonics perspective. *Nanophotonics*, 10(1):259–293, 2020. 1
- [96] Zhihong Zhang, Yuxiao Cheng, Jinli Suo, Liheng Bian, and Qionghai Dai. Infwide: Image and feature space wiener deconvolution network for non-blind image deblurring in low-light conditions. *IEEE Transactions on Image Processing*, 32:1390–1402, 2023. 3, 4
- [97] Guoxing Zheng, Holger Mühlenbernd, Mitchell Kenney, Guixin Li, Thomas Zentgraf, and Shuang Zhang. Metasurface holograms reaching 80% efficiency. *Nature Nanotechnology*, 10:308–312, 2015. 3
- [98] Yuqian Zhou, David Ren, Neil Emerton, Sehoon Lim, and Timothy Large. Image restoration for under-display camera. In *Proceedings of the IEEE/CVF conference on computer vision and pattern recognition*, pages 9179–9188, 2021. 4

# MetaFormer: High-fidelity Metalens Imaging via Aberration Correcting Transformers: Supplementary Materials

## A. Metalens Fabrication

### A.1. Fabrication Details

A metalens with a diameter of  $500\ \mu\text{m}$  and a focal length of  $1\ \text{mm}$  was designed based on the optimization of a polynomial phase equation [80]. The SiN meta-atom library was generated using rigorous coupled-wave analysis (RCWA) simulations for circular pillars with a height of  $750\ \text{nm}$ . The widths of the selected meta-atoms ranged from  $100$  to  $300\ \text{nm}$ , with a lattice period of  $350\ \text{nm}$ .

A  $750\ \text{nm}$  thick SiN layer was deposited onto a  $\text{SiO}_2$  substrate using plasma-enhanced chemical vapor deposition (PECVD; Oxford, PlasmaPro 100 Cobra) to fabricate the designed metalens. A  $200\ \text{nm}$  thick positive photoresist layer (AR-P 6200.09, Allresist) was spin-coated at  $4000\ \text{RPM}$ . The pattern of circular nano-pillar meta-atoms was then transferred onto the positive photoresist using electron beam lithography, as shown in Fig. 11 (a), with a dose of  $3.75\ \text{C}/\text{m}^2$ . To prevent charging,  $100\ \mu\text{L}$  of ESPACER (RESONAC, 300Z) was spin-coated at  $2000\ \text{RPM}$  for  $30\ \text{s}$ .

The exposed resist was developed in a 1:3 solution of methyl isobutyl ketone (MIBK)/isopropyl alcohol (IPA) for  $11\ \text{min}$ . Subsequently, a  $40\ \text{nm}$  thick chromium (Cr) layer was deposited as a hard mask using an electron beam evaporator (Fig. 11 (b)). The unexposed photoresist was removed through a lift-off process in acetone at room temperature for  $1\ \text{hour}$ , leaving the Cr hard mask intact. Patterning was finalized using inductively coupled plasma (ICP) etching (STS, multiplex ICP) with  $\text{SF}_6$  ( $15\ \text{sccm}$ ) and  $\text{C}_4\text{H}_8$  ( $40\ \text{sccm}$ ) gases for  $10\ \text{min}$ . Finally, the Cr hard mask was removed using a chromium etchant (TRANSENE, CE-905N) for  $5\ \text{min}$ . The fabricated metalens is illustrated in Fig. 12.

### A.2. Optical Setup for Imaging

An image capture setup is illustrated in Fig. 13. An optical microscope system was set up to obtain images through the metalens. The images displayed on a  $5.5$ -inch FHD display (FeelWorld, LUT5) were captured using a CMOS camera (Allied Vision, Alvium 1800 U-235c) coupled with a magnification system consisting of a  $20\times$  objective lens (Olympus, UPlanFL N  $20\times$ ) with  $0.5\ \text{NA}$  and a tube lens (Thorlabs, TTL180-A).

The metalens was positioned such that its focal plane coincided with the focal plane of the objective lens using a linear motorized stage (Thorlabs, DDS100). Camera exposure time was adjusted using a white image prior to recording to

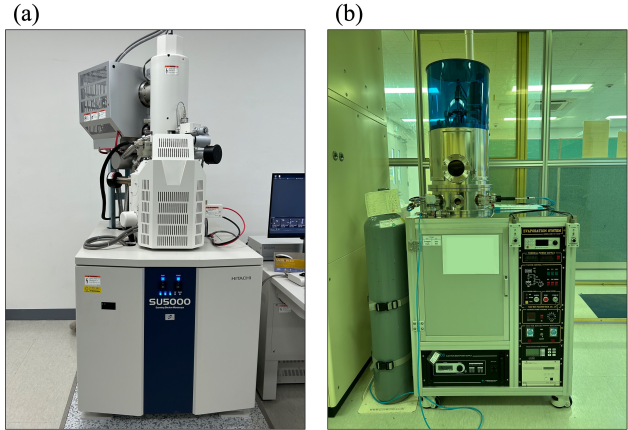


Figure 11. Equipments used for metalens fabrication. (a). Electron beam lithography system for high precision patterning of the metalens. (b). Electron beam evaporator to deposit a Cr layer as a hard mask during the fabrication process.

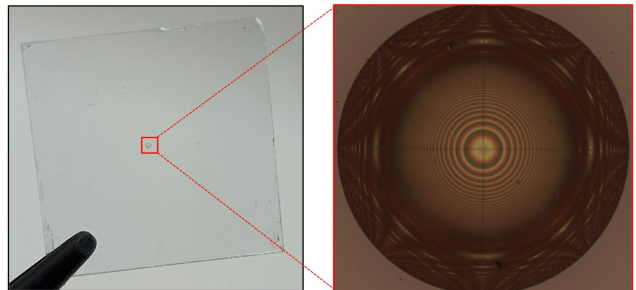


Figure 12. The fabricated metalens.

prevent saturation.

The point spread functions (PSFs) were then acquired using the same setup with  $450\ \text{nm}$  laser (Thorlabs, CPS450),  $532\ \text{nm}$  laser (Thorlabs, CPS532), and  $635\ \text{nm}$  laser (Thorlabs, CPS635) for calibration and training of the model.

## B. Additional Experiments and Results

In this section, we provide more experimental results on each task that were not delivered in the main paper due to the page limit. We also attached videos of the 3D reconstruction and video aberration correction task results.

**Evaluation Metrics.** We assessed the proposed method with various evaluation metrics including Peak Signal-to-Noise Ratio (PSNR), Structural Similarity Index Measure (SSIM) [84], and Learned Perceptual Image Patch Similar-

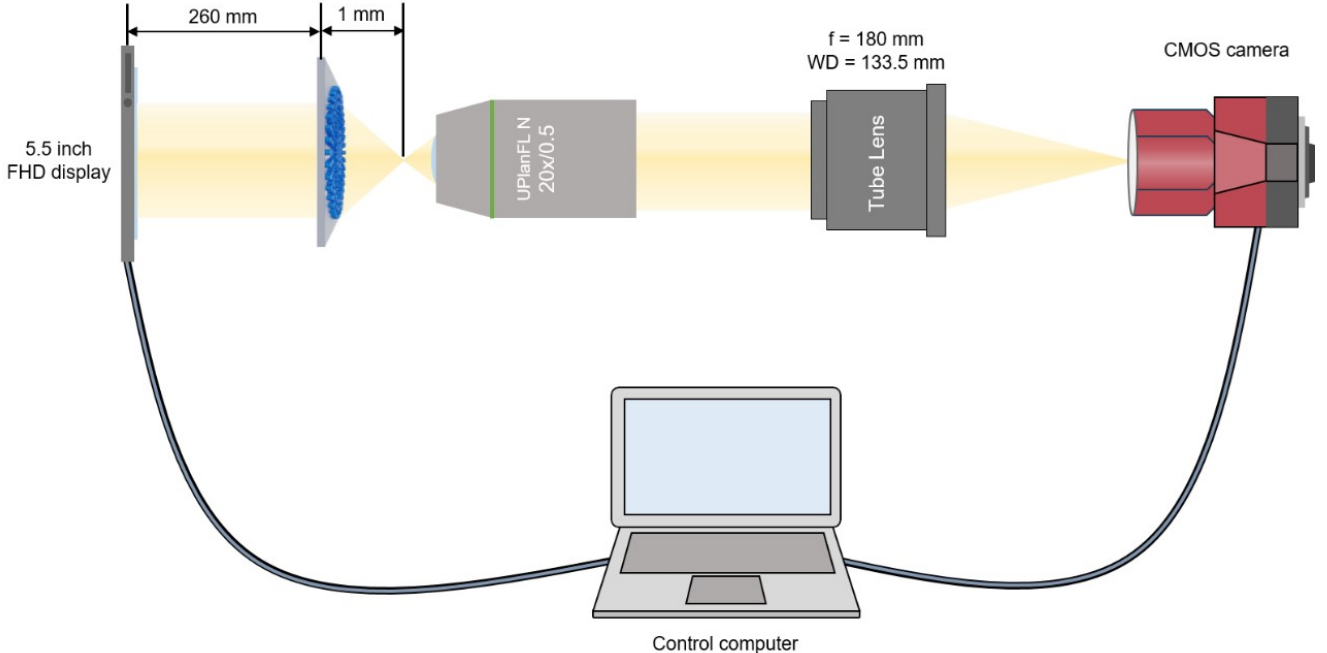


Figure 13. Experimental display imaging setup. The same setup was used to capture RGB PSFs.

ity (LPIPS) [94].

### B.1. Synthetic Image Aberration Correction

Fig. 14 shows extra qualitative results on the aberrated Open Image V7 [7, 48] dataset. The proposed method could mitigate severe aberrations and restore fine details. We also provide noise maps in Fig. 15 and Restormer [92] showed noises on textureless regions or failed to match contrast, where noise and low contrast are especially more prominent in metalens imaging. On the other hand, MetaFormer could alleviate noises and achieve the correct contrast, reaching better results on multiple evaluation metrics.

### B.2. Real Image Aberration Correction

**Model Fine-tuning Details.** We fine-tuned our model, initially trained on synthetically aberrated images in Sec. 4.2 in the main paper, using real images captured with the fabricated metalens. The fine-tuning dataset includes 200 real images for training and 20 images for validation. Despite the limited dataset size, fine-tuning MetaFormer for 3,500 iterations could produce promising and appealing results.

**Results.** Fig. 16 presents the qualitative results of images captured with the fabricated metalens and restored images using the proposed method. The captured images show harsh degradations and aberrations but MetaFormer could successfully restore fine details and textures. Such outcomes can demonstrate the adaptability of the proposed method to real-world scenarios.

### B.3. Video Aberration Correction

Fig. 17 shows additional qualitative results on the aberrated DVD [76] dataset. Similar to Fig. 8 in the main paper, the proposed method could effectively address aberrations in the video and produce aberration corrected representations.

### B.4. 3D Reconstruction with Aberrated Images

**More Method Details.** We used the combined loss function  $\mathcal{L}_{train}$ , consisting of  $\mathcal{L}_{abr}$  and  $\mathcal{L}_{ac}$  to train the proposed ‘3D-GS + MetaFormer’ as following:

$$\mathcal{L}_{train} = \mathcal{L}_{abr} + \lambda \mathcal{L}_{ac}, \quad (7)$$

where  $\lambda$  is a hyperparameter controlling weight of  $\mathcal{L}_{ac}$ . We used the pre-trained MetaFormer trained with the aberrated Open Image V7 [7, 48] dataset from Sec. 4.2 in the main paper to get aberration corrected images,  $I_{ac}$ .

**Experimental Settings.** For the LLFF [64] and Mip-NeRF360 [6] datasets, we set the densification threshold  $D$  of 3D Gaussian Splatting (3D-GS) model [41] to  $2e - 4$ , the pruning threshold  $P = 5e - 3$  and the loss weighting hyperparameter  $\lambda = 1.0$ . We also inactivated periodical opacity reset for the LLFF dataset to preserve more points in the forward-facing dataset [50]. We set  $D = 4e - 4$ ,  $P = 1e - 2$ , and  $\lambda = 2.0$  for the Tanks&Temples [44] dataset.

**Results.** We conducted experiments on the aberrated Mip-NeRF360 [6]. Tab. 5 and Fig. 18 show the quantitative and qualitative results, respectively. Training 3D-GS with the

Method	PSNR $\uparrow$	SSIM $\uparrow$	LPIPS $\downarrow$
3D-GS [41]	17.09	0.3270	0.8892
3D-GS w/ Ours	25.65	<b>0.6406</b>	0.4244
3D-GS + Ours	<b>25.66</b>	0.6395	<b>0.4201</b>

Table 5. Quantitative results on the aberrated Mip-NeRF360 [6] dataset.

# filters	PSNR $\uparrow$	SSIM $\uparrow$	LPIPS $\downarrow$
0	26.14	0.7231	0.3296
1	30.73	0.8065	0.2890
2	31.55	0.8108	0.2835
3	<b>32.01</b>	<b>0.8121</b>	0.2852
4	31.92	0.8111	<b>0.2804</b>

Table 6. Ablation study on the number of filters for MAFG.

output of MetaFormer (3D-GS w/ Ours) produced aberration alleviated representations but it suffered from artifacts due to the lack of multi-view consistency. In contrast, extra multi-view consistency guidance via  $\mathcal{L}_{abr}$  could aid in mitigating those artifacts from 3D inconsistency and yield more clear representations.

### B.5. More ablation studies

We conducted further ablation studies to demonstrate the effectiveness of the proposed methods. We evaluated all models after training 15K iterations.

**Comparison on the Number of Filters for MAFG.** Tab. 6 shows the results of comparing different numbers of involved filters in MAFG. The more filters we employed, the aberration correction performance was improved as it could enrich the input of the restoration network more. However, the performance dropped when we leveraged 4 filters in MAFG. We assume this is because excessive usage of filters may introduce over-redundancies and conflicting correlations within the representations, hampering correcting aberrations. Thus, we harnessed 3 filters in our experiments.

**Ablation on Using Intensity for MAFG.** We conducted an ablation study on using channel intensity information when defining filters for MAFG. We obtained multiple adaptive filters following Eq. (3) (MAFG) and simple multiple filters using Eq. (2) (MAFG w/o Intensity) in the main paper. We ran an experiment on a different test dataset, the aberrated DIV2K [1] dataset, to validate the adaptability of the proposed MAFG to unseen data. Exploiting channel intensity is simple, but it could impart the model flexibility to different images and facilitate aberration correction, especially showing a noticeable improvement in LPIPS as described in Tab. 7. We believe that a more sophisticated approach to incorporating image information, such as image intensity,

Method	PSNR $\uparrow$	SSIM $\uparrow$	LPIPS $\downarrow$
Restormer [92]	23.03	0.5872	0.4447
MAFG w/o Intensity	28.17	0.7305	0.4184
MAFG	<b>28.28</b>	<b>0.7357</b>	<b>0.3912</b>

Table 7. Ablation study on exploiting channel intensity in MAFG, evaluated on the aberrated DIV2K [1] dataset.

into the filters can further enhance the restoration process.

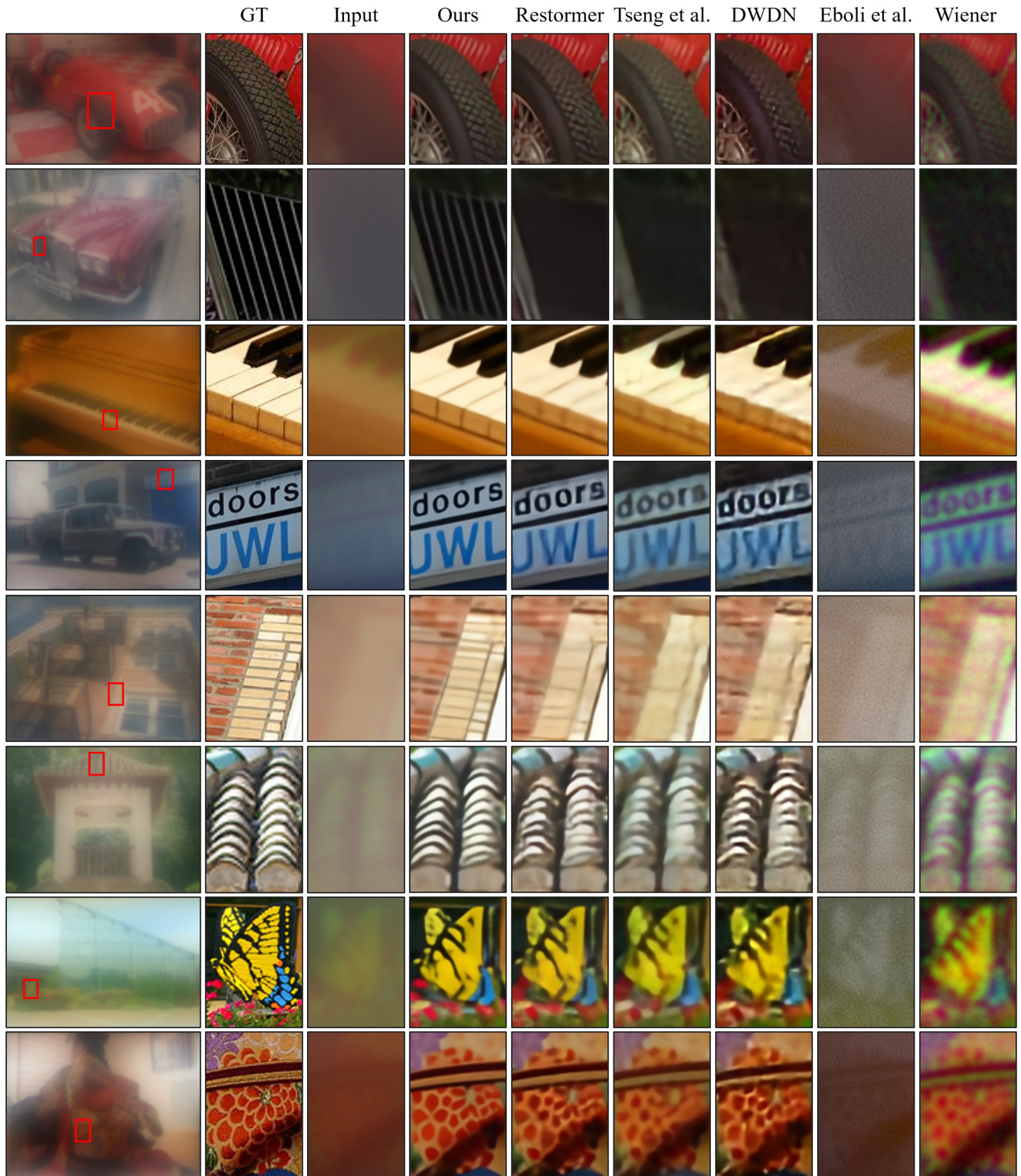


Figure 14. Additional qualitative results on the aberrated Open Image V7 [7, 48] dataset.

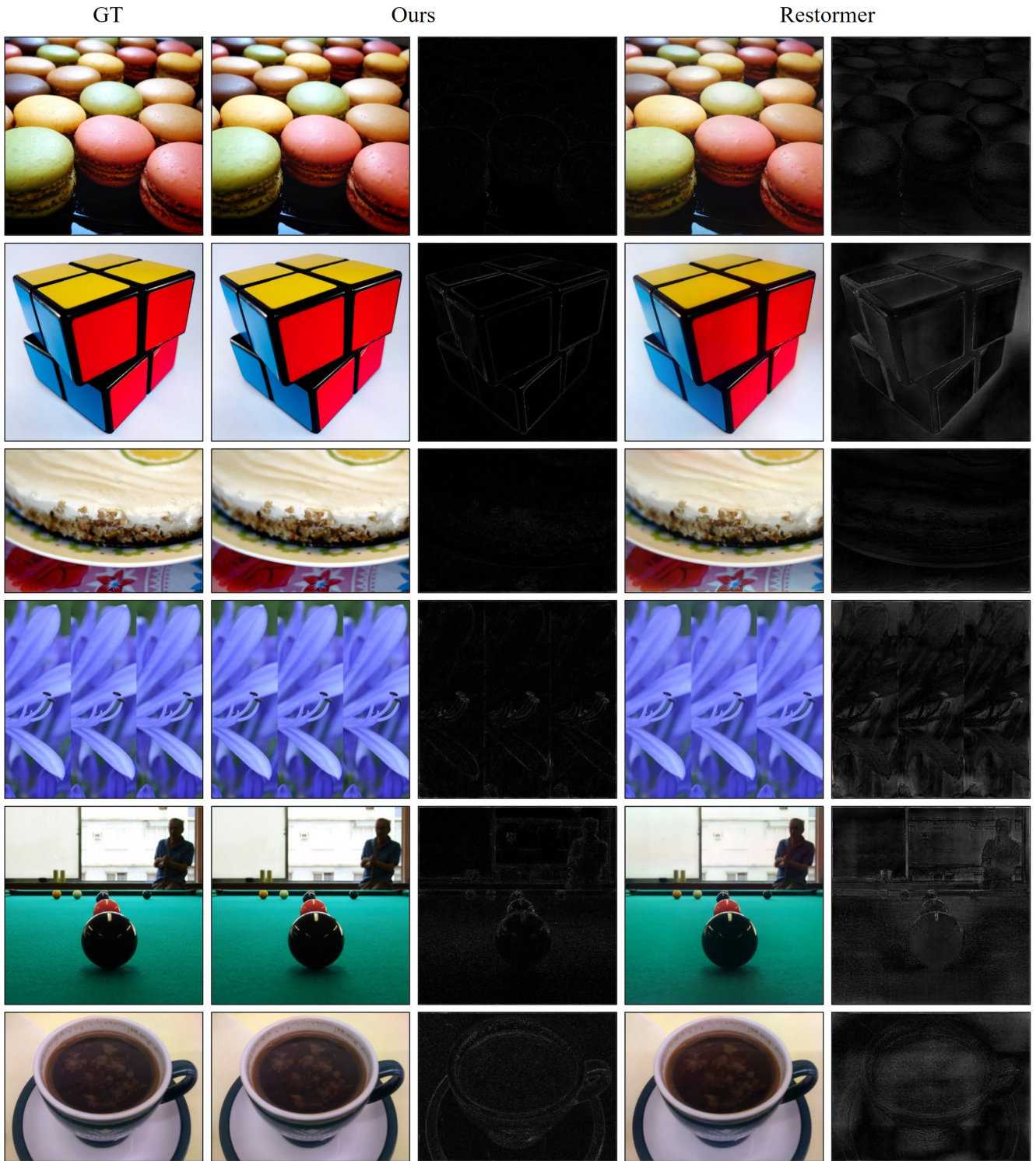


Figure 15. Restored images and noise maps on the aberrated Open Image V7 [7, 48] dataset. Images in the third and fifth columns show the computed noise maps. Noise maps are normalized for better visibility.

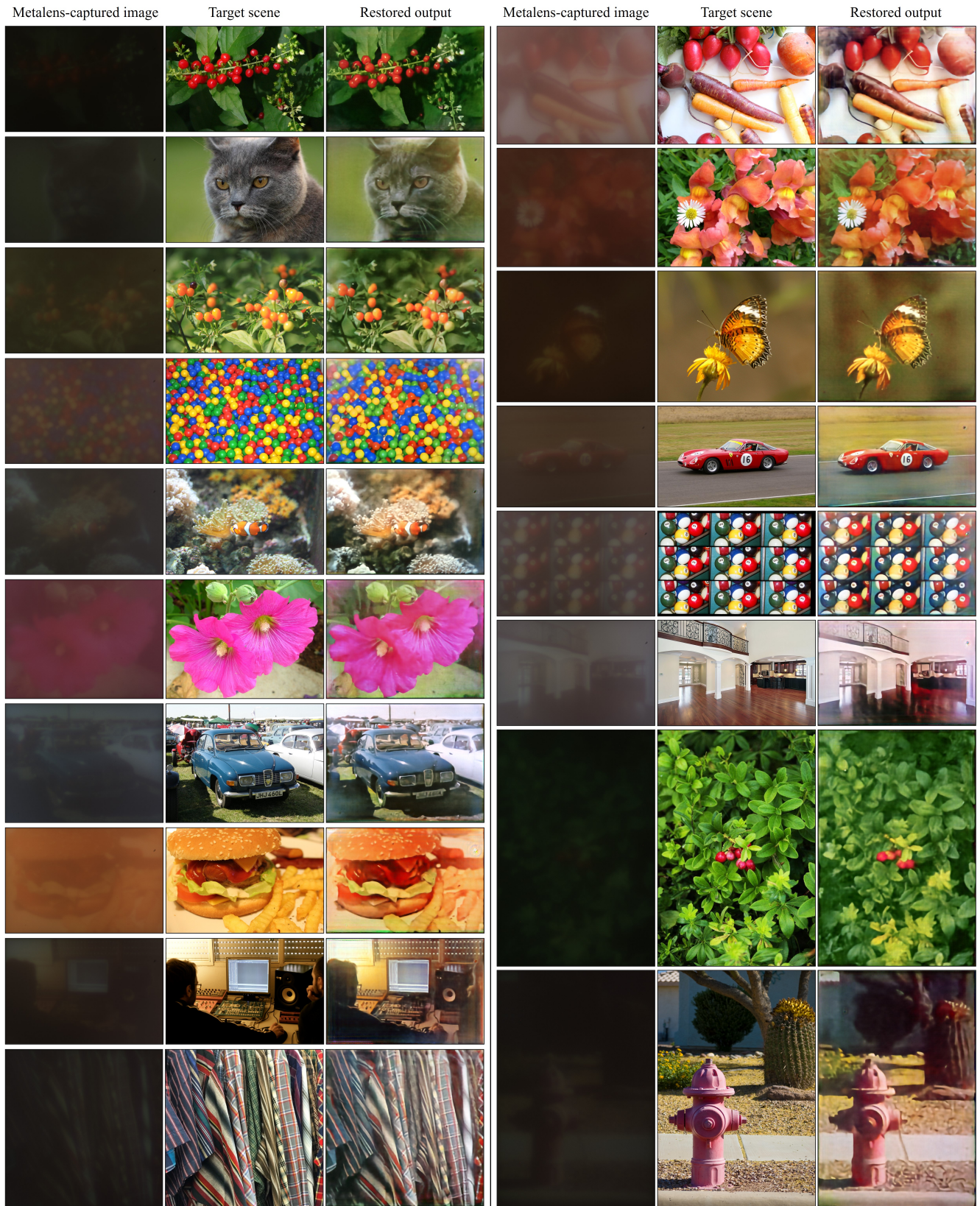


Figure 16. Additional qualitative results on the metalens-captured images.

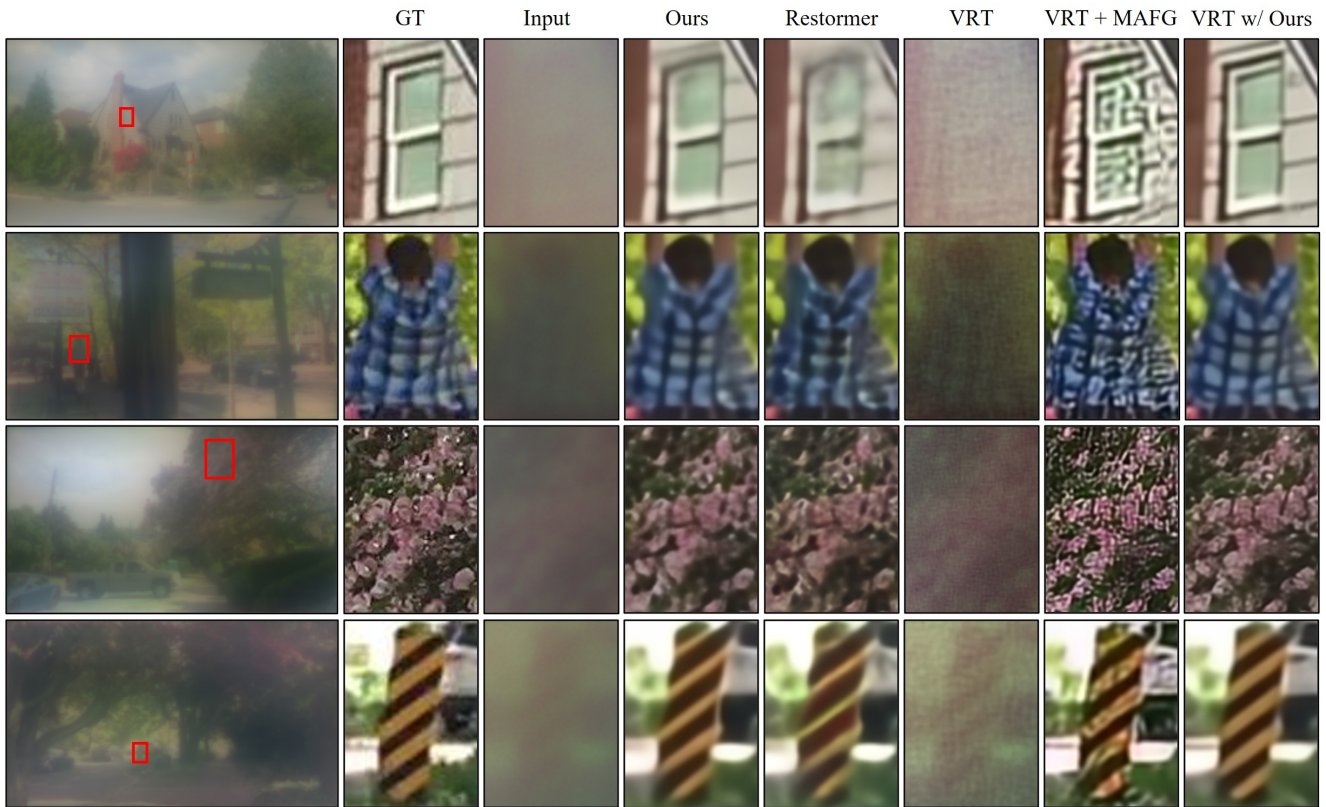


Figure 17. Additional qualitative results on the aberrated DVD [76] dataset.



Figure 18. Qualitative results on the aberrated Mip-NeRF360 [6] dataset.